Chemical Engineering Journal 439 (2022) 135536

Contents lists available at ScienceDirect

Chemical Engineering Journal

journal homepage: www.elsevier.com/locate/cej

One-pot synthesis strategy of sea urchin-like hollow microspheres comprising MoO_x nanorods attached *via* N-doped C as anodes for lithium-ion batteries

Jang Min Choi [1], Jae Seob Lee [1], Jung Sang Cho [*]

Department of Engineering Chemistry, Chungbuk National University, 1, Chungdae-Ro, Seowon-Gu, Cheongju-Si, Chungbuk 361-763, Republic of Korea

ARTICLE INFO

Keywords:
Molybdenum oxide
Hollow microsphere
Spray pyrolysis
Anodes
Lithium-ion batteries

ABSTRACT

A one-pot synthetic strategy that takes only 2.3 s was developed for the fabrication of sea urchin-like hollow microspheres comprising MoO_x nanorods attached *via* N-doped C for the first time. The inclusion of diethylenetriamine as a starting material played a key role in the formation of MoO_x nanorods constituting the hollow shell. Additionally, the MoO_x nanorods were coated and entangled with N-doped C, which established a rapid pathway for electrons and Li ions during the charge–discharge process when used as anodes for Li-ion batteries. Besides, numerous MoO_x nanorods grafted in the shell provided efficient one-dimensional electron transport along the longitudinal direction, enabling more efficient interaction with the Li-ions. Therefore, superior cycling performance was achieved: the nanostructure produced a discharge capacity of 794 mA h g^{-1} after 400 cycles at 0.2 A g^{-1} with a low decay rate of 0.074% per cycle. Discharge capacities of 891, 589, 358, 250, and 193 mA h g^{-1} were obtained at current densities of 0.5, 1.5, 3.0, 5.0, and 7.0 A g^{-1}, respectively. The facile synthetic strategy to prepare hollow microspheres using spray pyrolysis has important potential for the mass production of hierarchically hollow nanostructures in a wide range of fields, including energy storage.

1. Introduction

Hollow microspheres with diverse architectures have attracted considerable interest for both fundamental research and practical applications in a growing range of research fields, such as catalysts, gas sensors, drug delivery, and energy storage systems, because of their unique structural characteristics and physicochemical properties [1–5]. With regard to anode materials in lithium-ion batteries (LIBs), hollow microspheres also provide a greater surface area and more active sites for Li-ion adsorption and can shorten the diffusion pathways for Li ions and electrons during cycling [6-8]. Additionally, the inner hollow spaces can better tolerate the volume changes associated with the phase transitions that occur during the charge and discharge processes [6-8]. All of these factors can promote enhanced Li-ion storage capability and the stability of anode materials in LIBs [9-12].

Accordingly, extensive research efforts have been carried out to explore novel and facile synthetic strategies for the preparation of unique hollow microspheres that can reliably generate characteristic hollow structures [13-15]. One of the most representative methods, called the template-based route, directly replicates the shape of existing seeds, such as polymer or silica particles.[16] However, template-based routes are time consuming, have tedious operation, and provide low product yields, which restricts the practical use of these processes to fabricate hollow microspheres on large scales. On the other hand, template-free methods, including Oswald ripening, galvanic replacement, and Kirkendall diffusion processes, are alternative strategies that allow the synthesis of hollow structures through a simplified process without the preparation and removal of additional templates [17,18]. However, these processes involve additional post-treatment and require strict synthetic control.

Spray pyrolysis, which is an aerosol-assisted process, has gained prominence recently because it is a facile, cost-effective, and continuous process, and is thus commercially profitable [19-21]. In general, spray pyrolysis involves the atomization of droplets from a precursor solution using ultrasonic power followed by evaporation and decomposition in a thermal reactor. Because the spray pyrolysis process sprays micron-sized droplets from a solution with a desired ratio of precursor materials, it provides a homogeneous composition and spherical shape, which is

---

[*] Corresponding author.
E-mail address: jscho@cbnu.ac.kr (J.S. Cho).

[1] These authors contributed equally to this work.

https://doi.org/10.1016/j.cej.2022.135536
Received 30 November 2021; Received in revised form 4 February 2022; Accepted 26 February 2022

advantageous for synthesizing materials with desired morphologies and compositions with controlled stoichiometry [20]. However, the non-uniform sizes and morphologies of the as-prepared powders hinder their commercial application in powder synthesis, and many studies are being conducted to solve these problems. Therefore, studies exploring unique nanostructures obtained by controlling the parameters of the process and elucidating the synthetic mechanisms are necessary.

To the best of our knowledge, sea urchin-like hollow microspheres comprising MoO_x nanorods attached *via* N-doped C have been obtained for the first time in this study using spray pyrolysis as a one-pot process that takes only 2.3 s without any post-treatment. In particular, MoO_x is attracting attention as a promising anode for electrochemical energy storage devices due to its advantages of low cost, environmental friendliness, high theoretical capacity, and high electrochemical stability due to its layered structure [19,22,23]. However, the large volumetric expansion of MoO_x during the charge/discharge cycle results in poor cycling performance due to rapid capacity fading [19,24]. It is expected that the hollow MoO_x structure can achieve long cycle stability compared with filled structures because it accommodates sufficient space to sustain the volume changes associated with Li^+ insertion and extraction. However, the rapid transport of electrons is not ensured because of the low electrical conductivity of MoO_x, which results in polarization and eventually low reversible specific capacities [25]. To solve this problem, compositing with carbonaceous materials has been considered an effective strategy; however, this reduces the overall cell capacity [26,27]. Therefore, a minimum amount of C that allows for the transfer of electrons but does not reduce the cell capacity must be composited. Nevertheless, it remains challenging to design novel carbon hybrid materials with an optimum amount of C that can be obtained by a simple method without additional processes such as post-treatment.

In this study, MoO_x nanorods coated and entangled with an optimum amount of N-doped C are prepared by a facile one-pot process to obtain hollow shell structures that can provide rapid pathways for electrons and Li ions during the charge–discharge process. Numerous MoO_x nanorods constituting the shell provide efficient one-dimensional electron transport along the longitudinal direction, enabling more efficient interaction with the Li-ions. The formation mechanism of the unique nanostructure during spray pyrolysis is examined in detail by tracing the phases and morphological features of the structure based on the synthetic parameters. Additionally, the Li-ion storage properties of the unique nanostructure as an anode are comprehensively compared with those of filled-structure bare MoO_x microspheres and MoO_3 nanocubes.

2. Experimental section

Sample preparation: Sea urchin-like hollow microspheres comprising MoO_x nanorods attached *via* N-doped C (SUHM-MoO_x/NC) were prepared by a one-pot spray pyrolysis process. The spray solution was prepared by adding 0.3 M of $(NH_4)_6Mo_7O_{24}\cdot 4H_2O$ (DAEJUNG, >98.0%, Mw = 1235.86) and 27 g of PVP (DAEJUNG, Mw = 40,000) to 1.0 L of distilled water. Subsequently, 233 g of DETA (SAMCHUN, 98.5%, Mw = 103.17) was added to the solution and stirred vigorously to obtain a clear spray solution. Subsequently, the spray pyrolysis process was carried out to synthesize SUHM-MoO_x/NC using the prepared spray solution. The spray pyrolysis system used in this study is shown in Scheme S1. In the spray pyrolysis system, droplets were generated using a 1.7 MHz ultrasonic spray generator consisting of six vibrators. The droplets were carried to a quartz reactor (length = 1200 mm, diameter = 50 mm) by a carrier gas of air at a flow rate of 18 L min^{-1}. The reactor temperature was maintained at 800 ℃. For comparison, two types of bare MoO_x particles with filled structures were also prepared by spray pyrolysis. Filled bare MoO_3 nanocubes (F-MoO_3 nanocubes) were prepared by spray pyrolysis using an identical spray solution at a higher reaction temperature of 1000 ℃. In addition, filled MoO_x microspheres (F-MoO_x microspheres) were also prepared by spray pyrolysis using a spray solution containing only $(NH_4)_6Mo_7O_{24}\cdot 4H_2O$ without either PVP or DETA at 800 ℃.

Characterization techniques: The morphology of the samples was examined using FE-SEM (ULTRA PLUS, ZEISS) and field-emission transmission electron microscopy (FE-TEM; JEOL, JEM-2100F, KBSI). The phases and crystal structures of the samples were determined by XRD (D8 Discover with GADDS, Bruker) using Cu Kα radiation (I = 1.5418 Å). The chemical environment of the elements in the samples was determined by XPS (Thermo Scientific, K-Alpha) using monochromatic Al Kα radiation at 12 kV and 20 mA. Raman spectroscopy (Horiba Jobin-Yvon, HR800, LabRam) was conducted to investigate the crystallinity of the carbonaceous materials in the prepared samples. The surface area of the samples was measured using the BET method with N_2 as the adsorbate gas. Thermogravimetric analysis (TGA; Pyris 1, Perkin-Elmer) was carried out in an air atmosphere with increasing temperature from room temperature to 600 ℃ at a rate of 10 ℃ min^{-1} to quantify the carbon content.

Electrochemical measurements: The electrochemical properties of the samples were measured by constructing 2032-type coin cells. The working electrodes were composed of active material, conductive carbon (Super-P), and sodium carboxymethyl cellulose (CMC) as a binder at a mass ratio of 7:2:1. The electrodes were prepared using a slurry casting method on a copper foil, which was subsequently dried at 60 ℃ overnight in a hot air oven. Li metal and microporous polypropylene (PP) films were used as the counter electrode and separator, respectively. The electrolyte was composed of 1.0 M $LiPF_6$ in a mixture of fluoroethylene carbonate (FEC) and dimethyl carbonate (DMC) with a volume ratio of 1:1. The coin cell was assembled at room temperature in an Ar-filled glove box. The electrochemical performance of the samples was evaluated using CV, charge–discharge testing, and EIS. The voltage window throughout the electrochemical tests was fixed at 0.001–3.0 V. The CV measurements of the samples were carried out at a scan rate of 0.1 mV s^{-1}. The charge–discharge performance of the samples was measured at various current densities from 0.2 to 7.0 A g^{-1}. The EIS data for the samples were collected in the frequency range of 100 kHz to 0.01 Hz using a signal amplitude of 10 mV.

3. Results and discussion

The strategy for the formation mechanism of the sea urchin-like hollow microspheres comprising MoO_x nanorods attached with N-doped C is described in Scheme 1. The hierarchically structured hollow microspheres were prepared *via* a one-step spray pyrolysis process directly without any post-treatment, as shown in Scheme 1. Droplets containing an aqueous solution of homogeneously distributed molybdenum salt, polyvinylpyrrolidone (PVP) as a carbon source, and diethylenetriamine (DETA) were generated by an ultrasonic nebulizer during the spray pyrolysis process, as shown in Scheme 1-①. The droplets were then passed through a vertical quartz reactor tube maintained at 800 ℃ in an air atmosphere, resulting in the drying of the droplets and decomposition of Mo salt and DETA to form $MoO_6/NH_4^+/PVP/NH_4OH$ composite microspheres (Scheme 1-②). Subsequently, several reactions occurred simultaneously as the droplets passed through the reactor with a carrier gas, leading to the formation of the multi-phase MoO_x/C composite hollow microspheres, as shown in Scheme 1-③. The Mo salt in the composite was heterogeneously oxidized and grew to generate multiphase rod-shaped MoO_x (*h*-MoO_3, MoO_2, Mo_4O_{11}) crystals in the presence of DETA. The role of DETA is discussed in a later section. Concurrently, the continuous PVP phase in the sphere was decomposed to carbon and formed a hollow carbon matrix shell through the Ostwald ripening process. In the continuous reaction, the carbon shell matrix partially burned to optimize the amount of C in the composite, resulting in the coating and entanglement the MoO_x rods (Scheme 1-④). Additionally, MoO_x (*h*-MoO_3, MoO_2, Mo_4O_{11}) crystals were grown and converted to stable MoO_x phases, which finally created sea urchin-like hollow microspheres comprising MoO_x nanorods attached *via* N-doped C, as shown in Scheme 1-④. A series of powder formation mechanisms

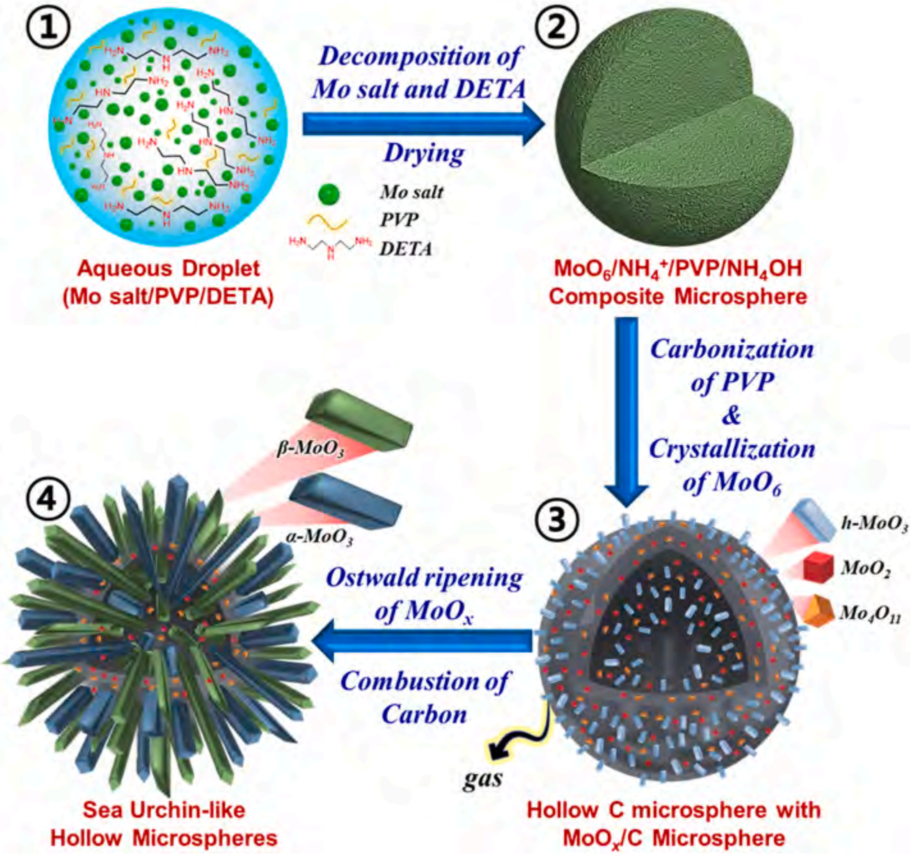

Scheme 1. Formation mechanism of the sea urchin-like hollow microspheres comprising MoO_x nanorods attached with N-doped C.

were completely progressed with a calculated residence time of only 2.3 s in a reactor, in this study.

In this study, MoO_x nanorods could be formed and designed as a part of the sea urchin-like hollow microspheres using a crystallographic strategy. The detailed formation mechanism of the 1-D rod-shaped MoO_x formed in the presence of DETA is proposed in Scheme 2. First, Mo salts in the aqueous system dissociated to $Mo_7O_{24}^{+}$ and NH_4^{+} ions, which then associated to form MoO_6 octahedral crystal units [28,29]. Concurrently, DETA as a key material was also decomposed into ammonia molecules (NH_3), which then formed hydrogen bonds with H_2O to produce ammonium hydroxide (NH_4OH) [30,31]. The molecular structure and functional groups of DETA are shown in Fig. S1. Therefore, MoO_6 octahedral crystals, NH_4OH, and residual ammonium ions (NH_4^{+}) were dispersed homogeneously in the droplets (Scheme 2-①). Subsequently, the MoO_6 crystals coalesced and self-integrated through the electrostatic attraction between their oxygen atoms and the NH_3 part of NH_4OH and NH_4^{+} ions in the droplet (Scheme 2-②). As the reaction progressed, the electrostatic repulsive force between the H_2O molecules of NH_4OH and the MoO_6 octahedra prevented the integration of MoO_6 units in the a-direction, resulting in anisotropic growth of hexagonal-phase MoO_3 (h-MoO_3) nuclei (Scheme 2-③). It is noteworthy that the H_2O part of NH_4OH played a role in the growth of the MoO_3 crystals along the z-axis, which could be achieved by adding DETA to the spray solution. Therefore, the h-MoO_3 nuclei were integrated continuously by Ostwald ripening and formed large 1-D rod-shaped h-MoO_3 (Scheme 2-③). To verify this formation mechanism of h-MoO_3 nanorods in the droplets during the spray pyrolysis process, a hydrothermal process was conducted using an aqueous solution containing Mo salt and DETA. The resulting product showed a rod-shaped particle with an h-MoO_3 phase (Fig. S2), which supports the formation mechanism described above. In Scheme 2-④, complete removal of both NH_4OH and NH_4^{+} ions occurred inside the h-MoO_3 structure as the reaction temperature increased. Finally, the metastable h-MoO_3 phase was converted to stable orthorhombic MoO_3 (α-MoO_3) and monoclinic MoO_3 (β-MoO_3) phases with 1-D rod shapes (Scheme 2-④).

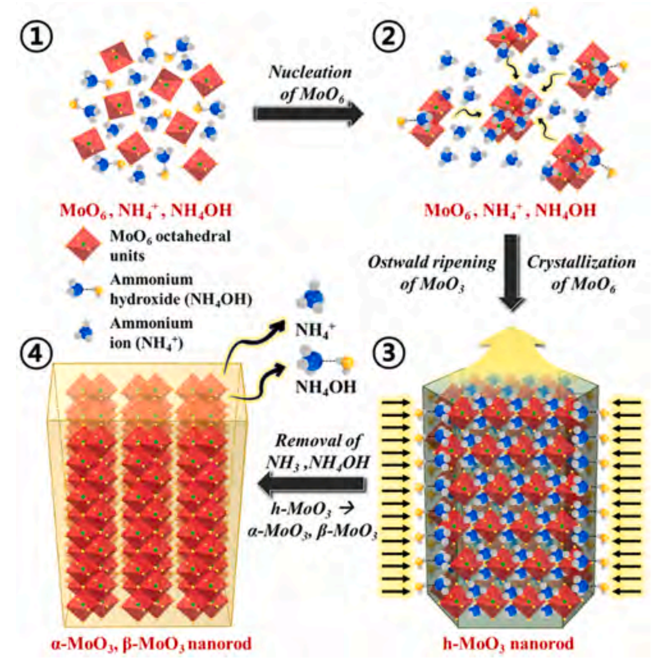

Scheme 2. Crystallographic mechanism for the formation of 1-D rod-shaped MoO_3 crystals comprising the microsphere.

To verify the synthetic mechanism of the unique sea urchin-like hollow microspheres during spray pyrolysis, the effects of both the reaction temperature and the additives on the powder morphology were investigated in detail. The morphologies of the as-prepared microspheres obtained with the spray solution containing Mo salt, PVP, and DETA at different reaction temperatures are shown in Fig. 1. As the reaction temperature was increased from 600 to 1000 ℃, the decomposition of Mo salt, PVP, and DETA and their chemical reactions occurred systemically. The aqueous droplet formed by the spray generator gradually dried as it passed through the reactor, and MoO_x crystals started to precipitate in the structure at 700 ℃ (Fig. 1c and d). Subsequently, 1-D rod-shaped crystals with various MoO_x phases were formed at 800 ℃, as shown in Fig. 1e and f. As elucidated in Scheme 2, the H_2O part of NH_4OH played a role in the growth of the MoO_3 crystals along the z-axis, which could be achieved by adding DETA to the spray solution. Therefore, the MoO_3 nuclei were continuously integrated and formed large 1-D rod-shaped MoO_3 crystals. At a higher reaction temperature of 900 ℃, the MoO_3 crystals in the structure were sintered, resulting in agglomeration of the MoO_3 rods as a lumped sphere (Fig. 1g and h). However, at temperatures above 1000 ℃, the carbon between the attached MoO_3 grains was completely decomposed into gas, causing the MoO_3 grains to separate and form independent MoO_3 nanocubes (Fig. 1i and j). In the X-ray diffraction (XRD) data (Fig. S3), as the reaction temperature increased from 600 to 1000 ℃, the peak intensity of the oxygen-deficient MoO_2 phase gradually decreased and was not observed at 1000 ℃, while the peak intensity of the oxygen-rich MoO_3 phase increased; only MoO_3 phases were confirmed at 1000 ℃. This is because the additives of PVP and DETA in the droplets produced a reducing atmosphere during the pyrolysis process at low reaction temperatures. Moreover, the change in the color of the as-prepared microspheres from black to greenish further confirmed the gradual removal of carbon from the structure. Therefore, sea urchin-like hollow microspheres could be obtained by entangling MoO_x nanorods with an appropriate amount of C at an optimum temperature of 800 ℃ in this study.

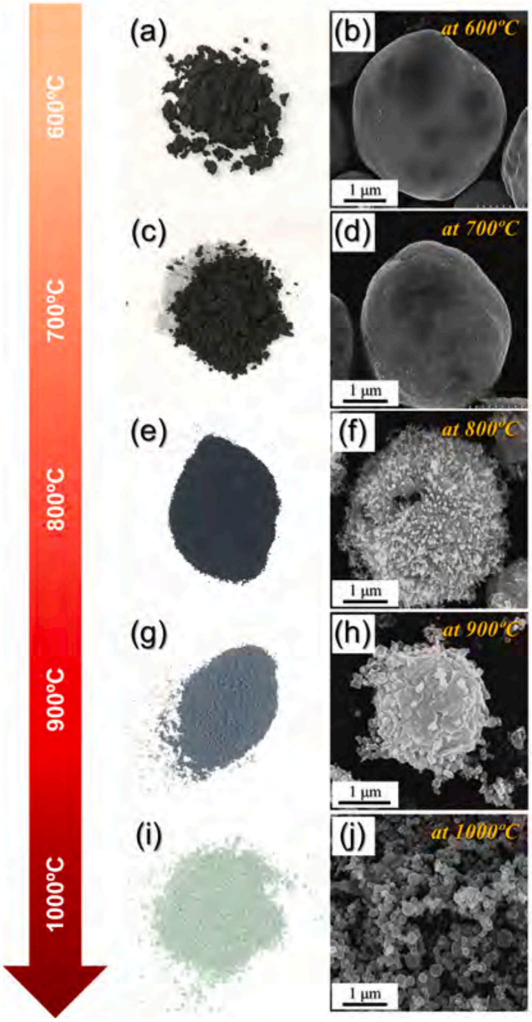

Fig. 1. Digital images, and morphologies of the as-prepared powders obtained after spray pyrolysis using the solution with Mo salt, PVP, and DETA at different temperatures: (a, b) 600 ℃, (c, d) 700 ℃, (e, f) 800 ℃, (g, h) 900 ℃, and (i, j) 1000 ℃.

The interaction between Mo salt, PVP, and DETA also had a significant effect on the microsphere morphology, as detailed in Fig. 2. The microspheres obtained from the solution containing only Mo salt were filled spherical structures (Fig. 2a and d). These filled microsphere structures were formed by the decomposition of metal salts and the homogeneous nucleation of MoO_x crystals in the droplets as a volume precipitation reaction at 800 ℃. MoO_3, an oxygen-rich phase, is generated preferentially on the surface of the sphere, while an oxygen-deficient Mo_9O_{26} phase is formed inside (Fig. 2g). When the PVP polymer was added to the Mo salt solution as an organic additive, a similar filled structure was obtained, as shown in Fig. 2b, e and h. However, the decomposition of PVP induced a reducing atmosphere in the powder system, resulting in the formation of oxygen-deficient MoO_2 and Mo_4O_{11} phases. Finally, the powders obtained using the solution with Mo salt and DETA showed microspheres comprising rod- and plate-shaped crystals, as shown in Fig. 2c and f. The rod-shaped crystals were formed in the presence of DETA in the spray solution. However, there was no carbon between the rods to suppress their agglomeration, resulting in the formation of bulky plates in the microspheres. Additionally, the reducing atmosphere formed by DETA decomposition during the process also affected the formation of oxygen-deficient MoO_2 and Mo_4O_{11} phases (Fig. 2i). In summary, sea urchin-like hollow microspheres comprising MoO_x nanorods attached *via* N-doped C could be prepared by controlling the reaction temperature and by the interaction between Mo salt, PVP, and DETA during the spray pyrolysis process.

The sea urchin-like hollow microspheres comprising MoO_x nanorods attached *via* N-doped C (SUHM-MoO_x/NC) prepared through the interaction of Mo salt, PVP, and DETA in a one-pot spray pyrolysis process at 800 ℃ are shown in Fig. 3. The SUHM-MoO_x/NC microspheres are spherical with a mean size of 2.4 μm and are composed of numerous nanorods with a width of 50 nm and a height of 200–500 nm, as shown in Fig. 3a–c. The transmission electron microscopy (TEM) image (Fig. 3d) exhibits a brighter part on the inside of the powder, which is attributed to the hollow structure, thus verifying that the nanorods formed are attached to each other and constitute a hollow shell. The fractured field emission scanning electron microscopy (FE-SEM) image shown in Fig. S4a further confirms that the hollow shell is composed of numerous nanorods. The H_2O part of NH_4OH in the droplet plays a role in the growth of MoO_x crystals along the z-axis in the presence of DETA during spray pyrolysis, thus forming 1-D rod-shaped MoO_3 crystals (Fig. 3e and f). The well-developed single crystal (Fig. 3f) grown along the longitudinal axis verifies this mechanism. The high resolution (HR)-TEM images shown in Fig. 3g reveal clear lattice fringes separated by distances of 0.38 nm and 0.40 nm, which correspond to the (1 1 0) crystal plane of α-MoO_3 and the (0 1 1) plane of β-MoO_3, respectively. Along with the two MoO_3 phases, oxygen-deficient MoO_2 and Mo_4O_{11} phases are also confirmed in the structure based on the selected area electron diffraction (SAED) pattern (Fig. 3h). The phase analysis is consistent with the XRD results for SUHM-MoO_x/NC, as shown in Fig. S3c. The Raman spectra shown in Fig. 3i also exhibit specific MoO_x characteristics. The two peaks at 991 and 816 cm^{-1} correspond to the stretching bond of Mo = O. The additional peaks at 661 cm^{-1}, 372 cm^{-1}, and 331 cm^{-1} are attributed to the stretching, scissoring, and bending of the O-Mo-O bond, respectively [32,33]. The elemental mapping data shown in Fig. 3j confirm the homogeneous distribution of elemental Mo,

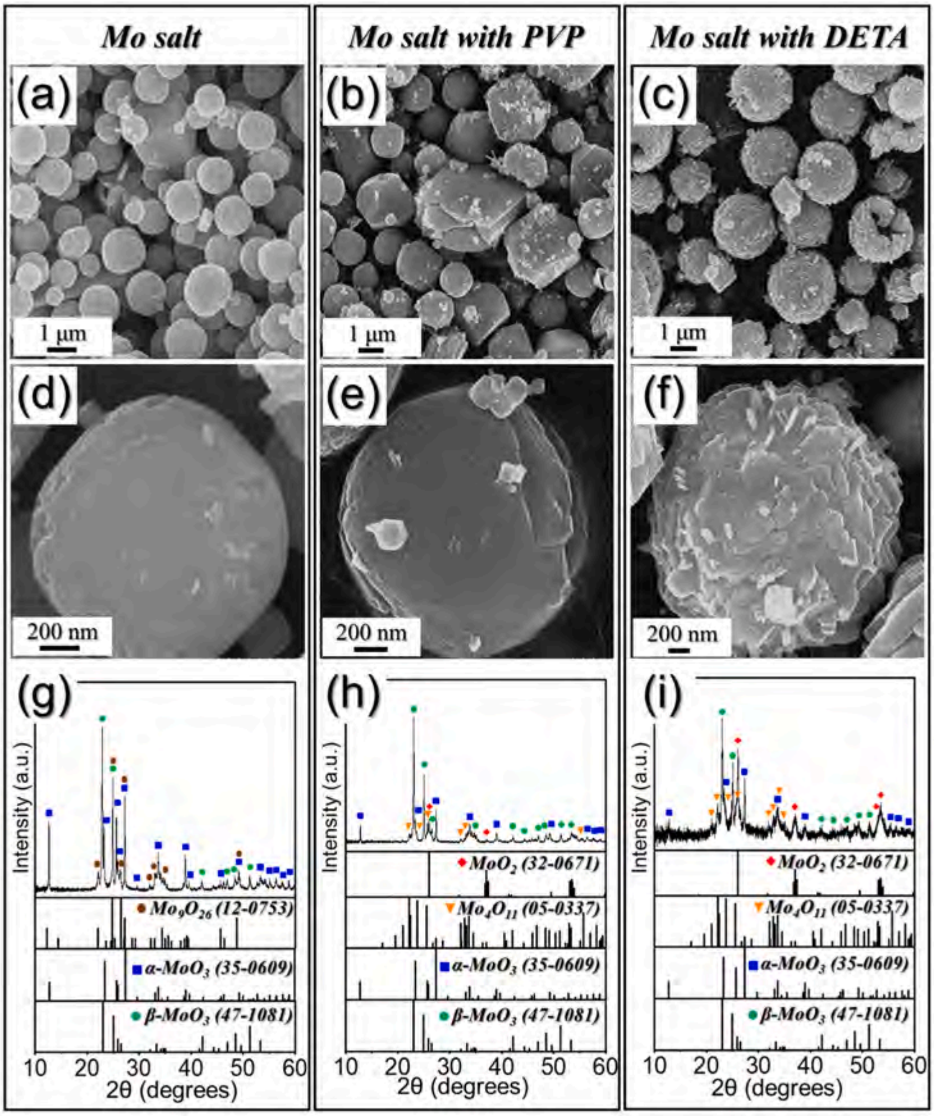

Fig. 2. FE-SEM images and XRD patterns of the as-prepared powders obtained after spray pyrolysis using the different solution with (a, d, g) Mo salt, (b, e, h) Mo salt and PVP, and (c, f, i) Mo salt and DETA.

O, C, and N throughout the structure, demonstrating the uniform formation of molybdenum oxides in the structure during the spray pyrolysis process. Additionally, C and N are also detected, which originate from the starting materials of Mo salt, PVP, and DETA as C/N sources. The N-doped C formed by PVP decomposition attaches the MoO_x nanorods to form the shell. To measure the degree of crystallinity of the carbon, the D- and G-bands of the Raman spectra were investigated (Fig. S4b). The relative intensity ratio (I_D/I_G) of the D- (1351 cm^{-1}) and G- (1594 cm^{-1}) bands is calculated as 1.42, indicating that the C coating and attaching to the MoO_x nanorods is mainly amorphous carbon.

The chemical nature of the SUHM-MoO_x/NC microspheres was analyzed *via* X-ray photoelectron spectroscopy (XPS), as shown in Fig. 4. The XPS survey spectrum (Fig. 4a) reveals the presence of Mo, O, C, and N. The high-resolution Mo 3d spectrum (Fig. 4b) exhibits two major peaks of Mo $3d_{5/2}$ and Mo $3d_{3/2}$ for Mo^{4+} and Mo^{6+} at 232.2 and 235.3 eV, respectively [19,34,35]. The Mo^{4+} peaks corresponding to binding energies of 231.4 and 234.4 eV indicate the presence of the MoO_2 phase. The Mo^{6+} peaks at 232.2 and 235.4 eV are attributed to the MoO_3 phase [19,34,35]. Moreover, the average valence calculated from the XPS peak areas of Mo^{4+} and Mo^{6+} was $Mo^{5.12+}$, and the ratio of MoO_2 and MoO_3 was 0.79. This result suggests that the predominant phase of MoO_x constituting SUHM-MoO_x/NC microspheres is MoO_3. The O 1 s spectrum shown in Fig. 4c exhibits three resolved peaks at binding energies at 530.1, 531.2, and 532.5 eV corresponding to Mo-O, O–H, and H_2O, respectively [36-39]. The C 1s spectrum (Fig. 4d) exhibits three peaks corresponding to the sp^2-bonded carbon (C = C), C–C/C-N, and C = O at 284.1, 285.5, and 288.0 eV, respectively [20,40-42]. The peak for the C-N bond at 285.5 eV confirms the N doping of C in the SUHM-MoO_x/NC microspheres [40]. The N 1s spectrum shown in Fig. 4e indicates the presence of two types of N species: pyridinic N at 398.0 eV and pyrrolic N at 400.7 eV [34,43-45]. In addition, a sharp peak at 396.0 eV is attributed to the Mo 3p orbital of the MoO_3 phase. The thermogravimetric (TG) curve for the SUHM-MoO_x/NC microspheres is shown in Fig. 4f. The weight increase starting at 330 ℃ is attributed to the conversion of MoO_2 and Mo_4O_{11} to the MoO_3 phase in the structure. The subsequent weight decrease at 420 ℃ is due to the combustion of N-doped C in the SUHM-MoO_x/NC microspheres. Based on the TG and elemental analysis (EA) (Table S1) results, the C and N contents in the SUHM-MoO_x/NC microspheres are estimated to be 3.9 and 2.7 wt%, respectively. The small amounts of N and C in the structures that attach the MoO_x nanorods to constitute the shell are expected to allow for the efficient transfer of electrons while not reducing the cell capacity during cycling.

To verify the structural merits of the SUHM-MoO_x/NC microspheres

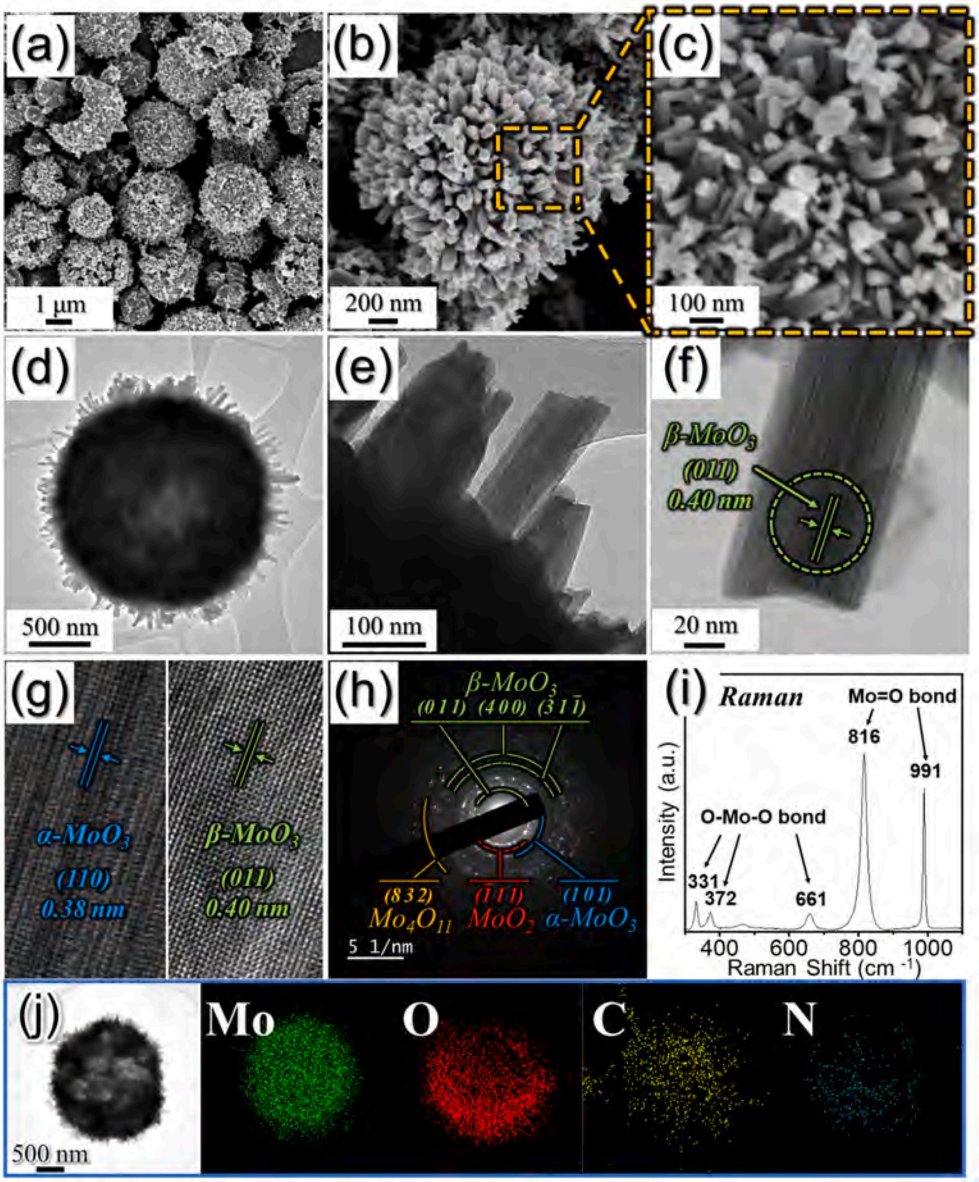

Fig. 3. (a-c) FE-SEM, (d-f) TEM, (g) HR-TEM images, (h) SAED pattern, (i) Raman spectrum, and (j) elemental mapping images of the SUHM-MoO_x/NC microspheres prepared by one-pot spray pyrolysis.

as anodes for LIBs, filled bare MoO_3 nanocube structures without C were also prepared through one-pot spray pyrolysis at a high reaction temperature of 1000 °C, as shown in Fig. 5. Furthermore, the formation mechanism of F-MoO_3 nanocubes was investigated through the morphology of powder obtained by controlling the flow rate of carrier gas from 40 to 5 L min^{-1} in the spray pyrolysis process fixed at 1000 ℃ (Fig. S5). Briefly, the droplets generated by the ultrasonic nebulizer pass through a vertical reactor to dry and decompose Mo salt and DETA to form MoO_6/NH_4^+/PVP/NH_4OH composite microspheres. However, due to the very high reaction temperature of 1000 ℃, NH_4^+ and NH_4OH vaporize quickly without any effect, PVP is carbonized, and MoO_6 is oxidized to MoO_3 nanocrystal. Finally, the carbon surrounding the MoO_3 crystal is removed and F-MoO_3 nanocubes are formed. The resulting product shows a cubic structure with a mean particle size of 198 nm, as measured from the FE- SEM and TEM images (Fig. 5a and b). The cubic shape is attributed to the intrinsic crystal growth mechanism of the orthorhombic and monoclinic MoO_3 phases in the droplet during the spray pyrolysis process. The HR-TEM image in Fig. 5c shows clear lattice fringes separated by 0.34 nm and 0.38 nm, corresponding to the (0 4 0) crystal plane of α-MoO_3 and the (0 1 1) crystal plane of β-MoO_3, respectively. The SAED pattern shown in Fig. 5d confirms that the as-prepared nanocubes contain both α-MoO_3 and β-MoO_3 phases, which is consistent with the XRD results in Fig. S3e. The MoO_3 nanocube without C is further confirmed by the absence of C in the elemental mapping images in Fig. 5e and the TG result (Fig. S6b). The Brunauer–Emmett–Teller (BET) surface areas of the SUHM-MoO_x/NC microspheres, filled MoO_3 nanocubes (F-MoO_3 nanocubes) shown in Fig. 5a, and filled MoO_x microspheres (F-MoO_x microspheres) shown in Fig. 2b are approximately 11, 9, and 10 m^2 g^{-1}, respectively (Fig. S7). The energy storage properties of these samples (F-MoO_3 nanocubes and F-MoO_x microspheres) are compared to verify the structural merits of the SUHM-MoO_x/NC microspheres.

The electrochemical performances of the SUHM-MoO_x/NC, F-MoO_3 nanocubes, and F-MoO_x microspheres are shown in Fig. 6. Fig. 6a shows the cyclic voltammetry (CV) results for the SUHM-MoO_x/NC microspheres over the first five cycles at a scan rate of 0.1 mV s^{-1} in the voltage window of 0.001–3.0 V. During the first cathodic scan, the broad peak at 1.85 V, which is only observed in the first cycle, is attributed to

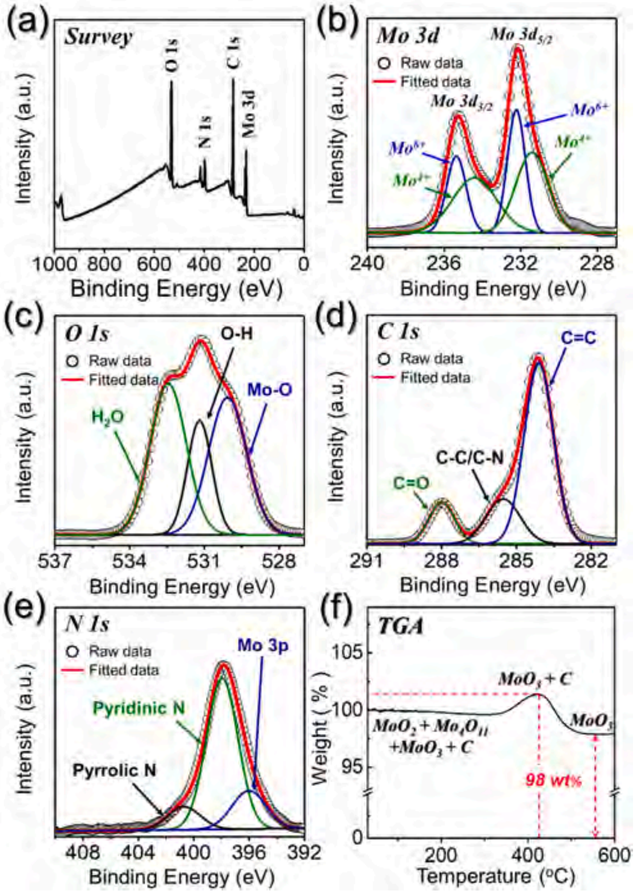

Fig. 4. Characteristics of the SUHM-MoO$_x$/NC microspheres: (a) XPS survey spectrum, (b) Mo 3d XPS spectrum, (c) O 1 s XPS spectrum, (d) C 1 s XPS spectrum, (e) N 1s XPS spectrum, and (f) TG curve.

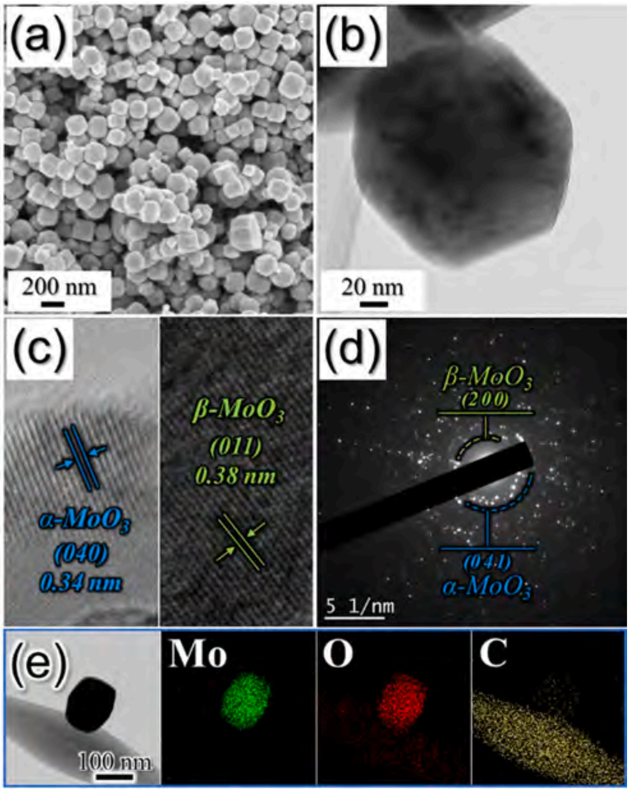

Fig. 5. (a) FE-SEM, (b) TEM, (c) HR-TEM images, (d) SAED pattern, and (e) elemental mapping images of the filled structured bare MoO$_3$ nanocubes prepared by spray pyrolysis at 1000 °C.

the intercalation of Li ions into the crystalline Mo_4O_{11} and MoO_3 phases to form Li_xMoO_x [46]. The two subsequent peaks at 1.43 V and 1.16 V are also attributed to the intercalation of Li ions into the MoO_2 crystals to form Li_xMoO_2 during Li insertion [47,48]. In addition, broad cathodic peaks at 0.21 V and 0.05 V suggest the conversion of Li_xMoO_x and Li_xMoO_2 to metallic Mo and Li_2O and the insertion of Li ions into the N-doped C, respectively [19]. During the first anodic scan, the peaks at 1.43 V and 1.73 V are attributed to the conversion of metallic Mo and Li_2O to MoO_2 and Li_xMoO_2 [47,48]. From the second cycle onward, the cathodic peaks for Li interaction with MoO_2 are shifted to slightly higher voltages owing to the formation of ultrafine nanocrystals of MoO_2, whereas the anodic peaks appear at the same potentials with slightly decreased intensities [47,48]. The overlapping CV curves after the first cycle suggest reversible redox processes. The F-MoO$_x$ microspheres and F-MoO$_3$ nanocubes show CV curves similar to those of SUHM-MoO$_x$/NC, as shown in Fig. S8. However, slightly different peaks are observed in the first cathodic scans of both samples. The several peaks distinguished between 2.67 V and 1.86 V in the initial cathodic curve of the F-MoO$_x$ microspheres (Fig. S8a) correspond to the multistep intercalation of Li ions into the crystalline MoO$_x$ phases to form Li_xMoO_x [46]. The peak at 2.55 V in the first cathodic curve of the F-MoO$_3$ nanocubes (Fig. S8b) is also attributed to the insertion of Li ions into crystalline MoO_3 to form Li_xMoO_3 [46]. A gradual decrease in the area of the CV curves for both F-MoO$_x$ microspheres and F-MoO$_3$ nanocubes as the cycling progresses demonstrates the formation of irreversible products during cycling.

The initial discharge–charge profiles of the samples at a current density of 0.2 A g^{-1} are shown in Fig. 6b. The obtained potential profiles are consistent with the CV results, with discharge and charge plateaus at 0.26 and 1.54 V, respectively. In addition, the initial discharge capacities of the SUHM-MoO$_x$/NC, F-MoO$_x$ microspheres, and F-MoO$_3$ nanocubes are 1638, 1664, and 1434 mA h g^{-1}, and the corresponding Coulombic efficiency (CE) values are 65%, 68%, and 67%, respectively. Although the SUHM-MoO$_x$/NC has carbon with a high initial irreversible capacity loss in its structure, there is no significant difference to the other structures in terms of the CE owing to the structural benefits of the SUHM-MoO$_x$/NC. Additionally, the SUHM-MoO$_x$/NC exhibits the lowest polarization potential ($\Delta V = 0.706$ V) compared to those of the F-MoO$_x$ microspheres ($\Delta V = 1.106$ V) and F-MoO$_3$ nanocubes ($\Delta V = 0.902$ V), as shown in Fig. S9. This clearly confirms the improved electronic and ionic conductivities of the SUHM-MoO$_x$/NC. The N-doped C coating and attachment of the MoO$_x$ nanorods constituting the hollow shell with efficient diffusion of charged species results in enhanced redox kinetics in the SUHM-MoO$_x$/NC, in this study.

The cycling performances of the samples at a current density of 0.2 A g^{-1} are shown in Fig. 6c. SUHM-MoO$_x$/NC shows a superior cycling performance compared to the F-MoO$_x$ microspheres and F-MoO$_3$ nanocubes over 400 cycles. The hollow and porous structure of SUHM-MoO$_x$/NC can efficiently absorb the mechanical stress induced by repeated Li ion diffusion during cycling. Moreover, the stability of the cycle performance is further improved due to the short diffusion length and stable crystal structure of Li-ions resulting from the molybdenum oxide nanorods [49]. The discharge capacity of the SUHM-MoO$_x$/NC is 794 mA h g^{-1} at the 400th continuous discharge/charge cycle, and the capacity decay rate measured from the second cycle is 0.074%. In addition, the initial capacity decrease of the SUHM-MoO$_x$/NC microspheres occurred due to the transformation of the crystal structure into a stable amorphous structure during cycling [50,51]. The subsequent gradual increase in discharge capacity is due to the formation of a polymer gel-like film on the active material, which is well known for most transition metal oxide anode materials [52,53]. In contrast, the discharge capacities of the F-MoO$_x$ microspheres and F-MoO$_3$ nanocubes continuously

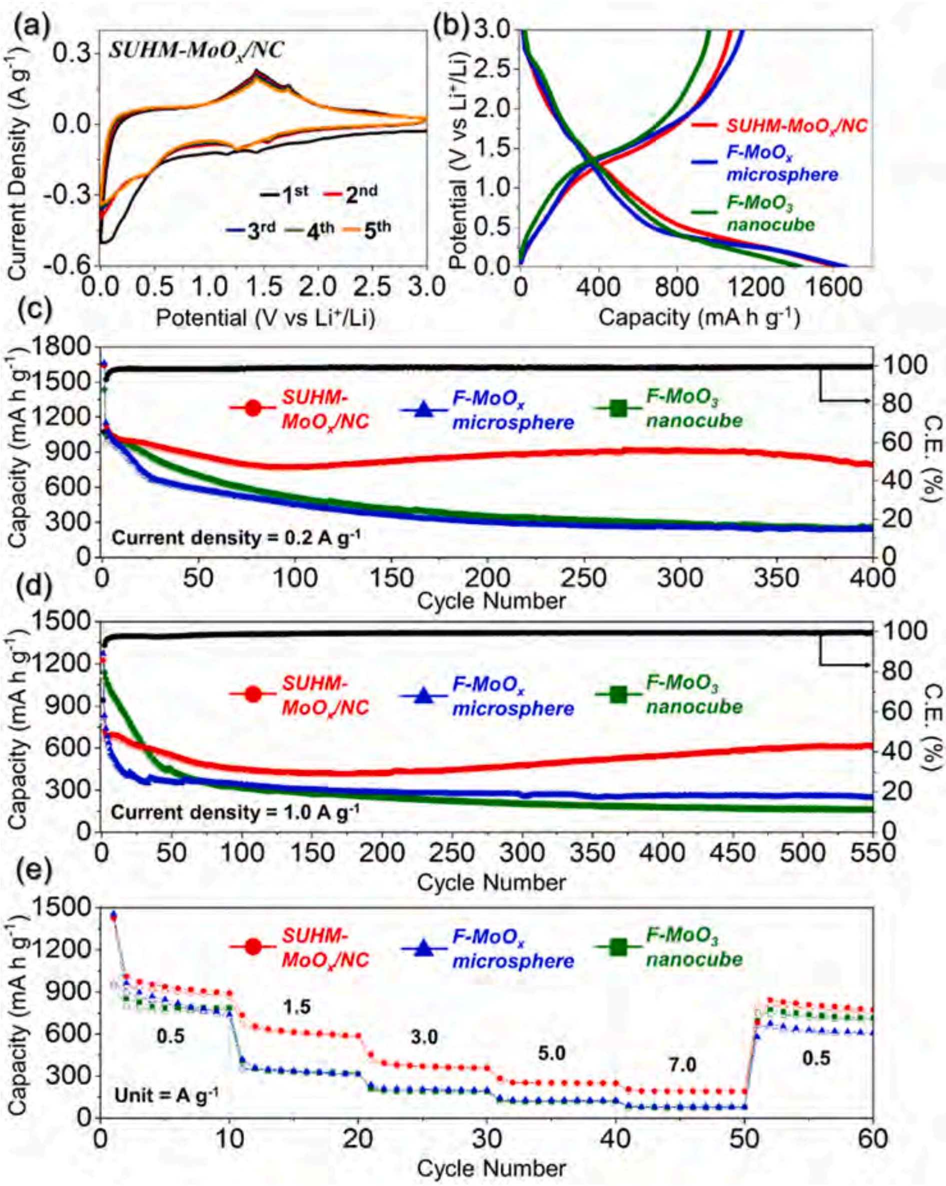

Fig. 6. Electrochemical properties of SUHM-MoO$_x$/NC microspheres, F-MoO$_x$ microspheres, and F-MoO$_3$ nanocubes: (a) CV curves of SUHM-MoO$_x$/NC microspheres, (b) initial discharge and charge profiles, (c) cycling performances at a current density of 0.2 A g^{-1}, (d) cycling performances at a current density of 1.0 A g^{-1}, and (e) rate performances.

decrease to 238 and 258 mA h g^{-1} in the 400th cycle, respectively, and the capacity decay rates measured from the second cycle are 0.1986% and 0.1888%, respectively. The large volume changes of the samples due to their filled structures are not accommodated during the repeated Li ion intercalation processes, eventually resulting in rapid capacity fading. Fig. 6d shows the cycling performances of the samples at a higher current density of 1.0 A g^{-1}. In the first tens of cycles, SUHM-MoO$_x$/NC and F-MoO$_x$ microspheres show lower discharge capacity than F-MoO$_3$ nanocubes. This is due to the MoO$_2$ crystal phase observed through XRD results (Fig. S3c and Fig. 2h), and it has already been reported that MoO$_2$ exhibits low theoretical discharge capacity as compared to MoO$_3$ [48]. However, SUHM-MoO$_x$/NC shows stable discharge capacities even at high current density, with a discharge capacity of 618 mA h g^{-1} at the 550th cycle due to its structural advantage. In contrast, the F-MoO$_x$ microspheres and F-MoO$_3$ nanocubes show sharp declining slopes and discharge capacities of 248 and 162 mA h g^{-1}, respectively, at the 550th cycle. The high specific capacities and stable cycling performance of SUHM-MoO$_x$/NC are attributed to the following structural benefits: (1) the hollow and porous structure can accommodate large volumetric deformations; (2) the presence of N-doped C with high electrical conductivity induces rapid charge transfer during cycling; and (3) the MoO$_x$ nanorods constituting the shell enable fast Li-ion diffusion.

The rate performances of the samples are shown in Fig. 6e for current densities increasing stepwise from 0.5 to 7.0 A g^{-1}. The final discharge capacities of the SUHM-MoO$_x$/NC at current densities of 0.5, 1.5, 3.0, 5.0, and 7.0 A g^{-1} are 891, 589, 358, 250, and 193 mA h g^{-1}, respectively. When the current density is reduced to 0.5 A g^{-1} again, the discharge capacity of the SUHM-MoO$_x$/NC recovers well to 843 mA h g^{-1}. The capacities of the SUHM-MoO$_x$/NC are much higher than those of the F-MoO$_x$ microspheres and F-MoO$_3$ nanocubes, which exhibit discharge capacities of 787/740, 313/315, 201/190, 128/120, and 81/75 mA h g^{-1}, respectively, at identical current densities. The high-rate performance of the SUHM-MoO$_x$/NC also confirms its structural superiority for LIBs compared with the filled structures. Numerous MoO$_x$ nanorods comprising a shell enhance the charge transfer kinetics via longitudinal pathways, which in turn promotes fast electrochemical reactions. Additionally, an optimum amount of N-doped C with high electrical conductivity used to coat and attach the MoO_x nanorods can facilitate rapid electron transfer during cycling. Moreover, the obtained electrochemical in the present work performance are comparable to the previous works, as presented in Table S2.

The superior performance of the SUHM-MoO_x/NC is further elucidated by comparing the lithium-ion diffusion coefficients (D_{Li^+}) of the samples. All cells were cycled from 0.1 to 2.0 mV s^{-1}, and the corresponding CV curves are shown in Fig. 7a, c, and e. There are two cathodic peaks labeled "peak 1" at 1.45 V and "peak 2" at 1.23 V, and two anodic peaks marked as "peak 3" at 1.48 V and "peak 4" at 1.75 V in the CV curves. These peaks are attributed to the electrochemical interaction of MoO_2 formed during the revisible phase transition with Li ions. The lithium-ion diffusion coefficient (D_{Li^+}) is calculated using the Randles–Sevcik equation (Eq. (1)) [54].

$$I_p = 2.69 \times 10^5 n^{1.5} A D_{Li^+}^{0.5} C_{Li} \nu^{0.5} \tag{1}$$

where D_{Li^+} is the lithium-ion diffusion coefficient (cm^2 s^{-1}), I_p is the cathodic/anodic peak current (A), n is the number of electrons involved in the reaction (n = 4), A is the electrode area (cm^2), C_{Li} is the lithium-ion concentration (mol L^{-1}), and ν is the scan rate (V s^{-1}). Plots showing the relationship between the cathodic/anodic peak current, I_p, and the square root of the scan rate ($\nu^{0.5}$) for the three different structures are shown in Fig. 7b, d, and f, and the obtained values are listed in Table S3. The average diffusion coefficient values for the SUHM-MoO_x/NC, F-MoO_x microspheres, and F-MoO_3 nanocubes are calculated as 3.29×10^{-10}, 2.48×10^{-10}, and 1.38×10^{-10} cm^2 s^{-1}, respectively. SUHM-MoO_x/NC shows the highest D_{Li^+} value of the samples, indicating faster Li ion diffusion and thus superior redox reaction kinetics during the charge–discharge process, which ultimately contributes to the increased energy storage performance of the SUHM-MoO_x/NC.

To better understand the electrochemical dynamics inside the cell, the CV curves are plotted for SUHM-MoO_x/NC microspheres in voltage windows of 0.001–3.0 V at different scan rates, as shown in Fig. 8a. In addition, the graphs were plotted between the peak current (i) and the scan rate (v) during reduction/oxidation according to the following power law relationship to distinguish the capacitive- and diffusion-controlled processes in the CV curve [55-57]:.

$$i = av^b \tag{2}$$

$$\log(i) = b\log(v) + \log(a) \tag{3}$$

Here, variables a and b determine whether the process is diffusion-controlled or capacitive-controlled. The redox process is mainly capacitive-controlled when b approached 1.0 whereas it is mainly diffusion- controlled when b approached 0.5 [55-57]. The b values were determined using the slopes of log(i) versus log(v) plots for different cathodic and anodic peaks. The calculated b values at different redox peaks for the three structures are shown in Fig. 8b and S10. The b values for the four different redox peaks in the SUHM-MoO_x/NC microspheres were 0.90, 0.84, 0.77, and 0.79, indicating a capacitive-dominant process. In contrast, the F-MoO_x microspheres and F-MoO_3 nanocubes shown in Fig. S10 indicate low b values close to 0.5, suggesting that the diffusion-controlled process during charging and discharging is the dominant factor. In general, the capacitive effect of the electrode material is closely related to the reaction kinetics, implying that the higher the percentage of the capacity control process, the better the transport kinetics. Therefore, for the quantitative analysis of the capacitive contribution to the current response, the total stored charge in the electrode material was separated into capacitive and diffusion-

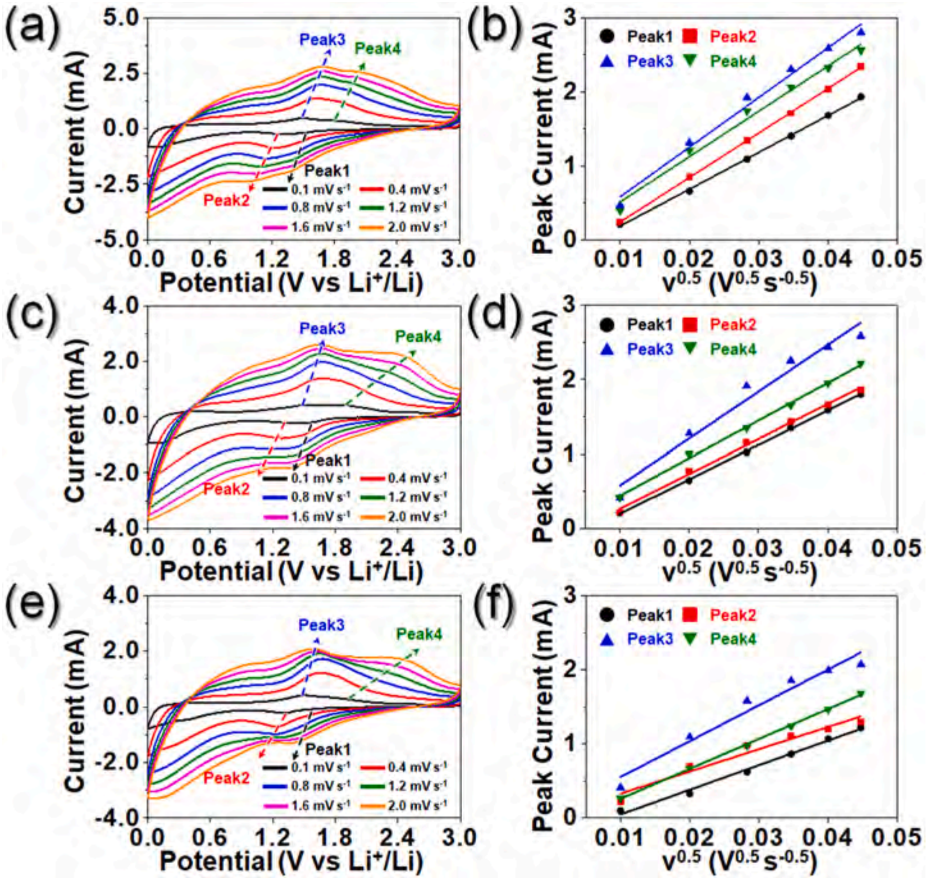

Fig. 7. CV curves and their corresponding linear fits to the peak current values of samples: (a, b) SUHM-MoO_x/NC microspheres, (c, d) F-MoO_x microspheres, (e, f) F-MoO_3 nanocubes.

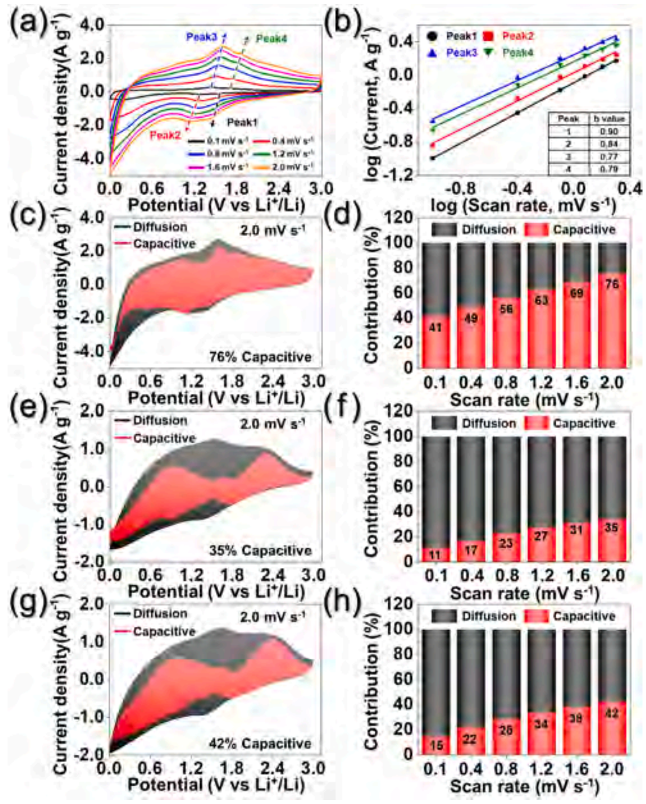

Fig. 8. Electrochemical reaction dynamics analysis of (a-d) SUHM-MoO$_x$/NC, (e and f) F-MoO$_x$ microspheres, and (g and h) F-MoO$_3$ nanocubes: (a) CV curves obtained at various scan rates, (b) current response (i) vs. scan rate (n) at each redox peak, (c, e, and g) CV curves with the capacitive fraction shown by the red region at a scan rate of 2.0 mV s^{-1}, and (d, f, and h) bar charts showing the percentage of the capacitive contribution at different scan rates.

controlled processes using the following equations [58,59]:.

$$i = k_1 v + k_2 v^{1/2} \tag{4}$$

where $k_1 v$ and $k_2 v^{1/2}$ are the capacitive and diffusion contributions, respectively, and k_1 and k_2 are the constants obtained from the slope and intercept of the $i(V)/v^{1/2}$ vs $v^{1/2}$ plot, respectively [58,59]. As shown in Fig. 8c, the capacitive contribution coefficient ($k_1 v$) of the SUHM-MoO$_x$/NC microspheres highlighted by the red region is 76% at a scan rate of 2.0 mV s^{-1}. Fig. 8d shows the capacitive fraction of SUHM-MoO$_x$/NC microspheres at scan rates other than 2.0 mV s^{-1}. In contrast, the contribution of the surface-controlled reaction in the F-MoO$_x$ microspheres and F-MoO$_3$ nanocubes shown in Fig. 8e and f and Fig. 8g and h, respectively, suggest a lower percentage of the capacitive process compared to the SUHM-MoO$_x$/NC microspheres. These results suggest that numerous MoO$_x$ nanorods including shells offer efficient one-dimensional electron transport along the longitudinal direction, which enable more efficient interaction with Li-ions. Besides, an optimal amount of N-doped C with high electrical conductivity surrounding MoO$_x$ nanorods can promote fast electron transport.

The excellent Li-ion storage properties of SUHM-MoO$_x$/NC are further verified based on electrochemical impedance spectroscopy (EIS) measurements of the cells before and after the first and 100th cycles in a fully charged state, as shown in Fig. 9 [10,22,60]. EIS measurements were carried out using the deconvolution Randle-type equivalent-circuit model of the cell shown in Fig. 9a, and the measured resistance values of the three prepared structures are summarized in Table S4. The Nyquist plots for fresh cells (Fig. 9b) suggest marginally different solution resistance (R$_s$) values in the range of 24–39 Ω, indicating slightly different electrode–electrolyte interface responses. Furthermore, the

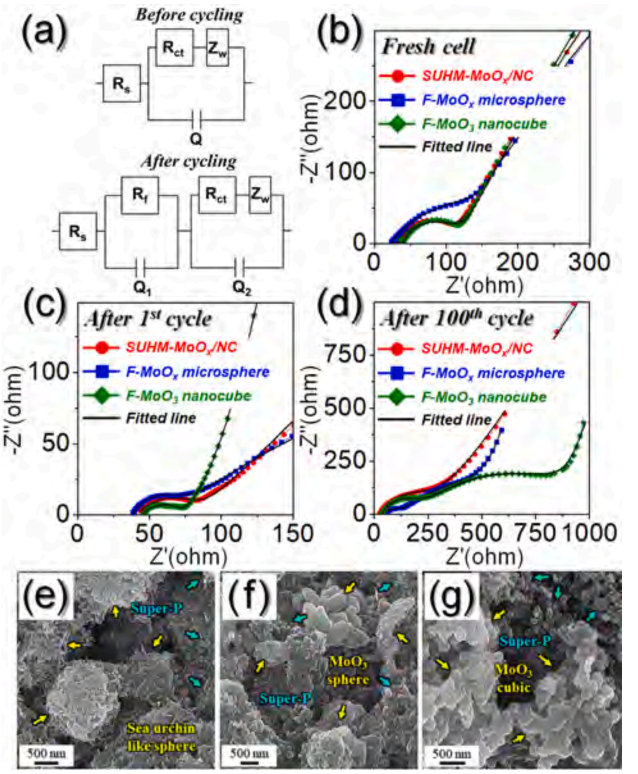

Fig. 9. (a) equivalent circuit model used for AC impedance fitting before cycling, and after cycling, R$_{ct}$ = charge-transfer resistance, R$_s$ = solution resistance, R$_f$ = SEI layer resistance, Q$_1$ = dielectric relaxation capacitance, Q$_2$ = associated double layer capacitance, (b-d) Nyquist impedance plots: (b) before cycling, (c) after 1st cycle, (d) after 100th cycle, (e-g) FE-SEM images of samples obtained after 100th cycles at 0.2 A g^{-1}: (e) SUHM-MoO$_x$/NC microspheres, (f) F-MoO$_x$ microspheres, and (g) F-MoO$_3$ nanocubes.

charge transfer resistance (R$_{ct}$) values of the SUHM-MoO$_x$/NC, F-MoO$_x$ microspheres, and F-MoO$_3$ nanocubes are 103, 228, and 100 Ω, respectively (Fig. 9b). The micron-sized filled structure of the F-MoO$_x$ microspheres affects the increase in the R$_{ct}$ value of the cell. However, after the first cycle, all of the samples exhibit a substantial decrease in R$_{ct}$ (SUHM-MoO$_x$/NC: 48 Ω, F-MoO$_x$ microspheres: 49 Ω, and F-MoO$_3$ nanocubes: 22 Ω), which is due to the formation of ultrafine MoO$_2$ crystals in the structure after the first cycle (Fig. 9c) [25]. In addition, all three structures began to observe film resistance (R$_f$) due to the formation of a solid electrolyte interface (SEI) layer. After the 100th cycle, the SUHM-MoO$_x$/NC shows the lowest R$_{ct}$ value of 314 Ω compared to the F-MoO$_x$ microspheres (848 Ω) and F-MoO$_3$ nanocubes (973 Ω), suggesting fast redox kinetics and superior electrode integrity of the SUHM-MoO$_x$/NC (Fig. 9d) even after 100 cycles. To confirm the structural integrity of the SUHM-MoO$_x$/NC, the morphologies of the samples after the 100th cycle at a current density of 0.2 A g^{-1} are shown in Fig. 9e, f, and g. The SUHM-MoO$_x$/NC (Fig. 9e) after cycling exhibits a microsphere morphology with MoO$_x$ nanorods on the surface. The hollow and porous structure can accommodate the structural stress caused by the large volume variation in the MoO$_x$ constituting the shell induced by Li-ion diffusion during repeated cycling. Moreover, the stability of the cycle performance is further improved due to the short diffusion length and stable crystal structure of Li-ions resulting from the molybdenum oxide nanorods. However, the F-MoO$_x$ microspheres and F-MoO$_3$ nanocubes (Fig. 9f and g) exhibit complete structural degradation into bulk agglomerates after cycling owing to their inability to withstand the volume variation. These results confirm the high structural robustness of the SUHM-MoO$_x$/NC, leading to the superior cycling properties of the cell in this study. Overall, the outstanding Li-ion storage properties of the cells are achieved because of the synergistic effects of the SUHM-MoO$_x$/NC microspheres proposed in this study. The unique hollow and porous structure alleviate the large volumetric variation and allow the penetration of electrolytes into the structure. Moreover, the N-doped C coating and attaching the MoO_x nanorods contributes to an increase in the electrical conductivity of the electrode, inducing rapid charge transfer during cycling. Finally, the MoO_x nanorods constituting the shell enable fast Li-ion diffusion that subsequently favored the fast redox kinetics.

4. Conclusions

As high-performance anodes for lithium-ion batteries, sea urchin-like hollow microspheres comprising MoO_x nanorods attached *via* N-doped C were designed and synthesized using a one-pot spray pyrolysis process. In this strategy, the inclusion of DETA as a starting material played a key role in the formation of the MoO_x nanorods constituting the hollow shell. DETA was decomposed into ammonia molecules (NH_3), which formed hydrogen bonds with H_2O to produce ammonium hydroxide (NH_4OH). The H_2O part of NH_4OH played a role in the growth of MoO_x crystals along the z-axis; therefore, the MoO_x nuclei were integrated and formed large 1-D rod-shaped MoO_x. The MoO_x nanorods were coated and entangled with N-doped C, which established a rapid and efficient pathway for electrons and Li ions during the charge–discharge process. Additionally, MoO_x nanorods constituting the hollow shell facilitated the penetration of electrolyte and enhanced the diffusion of charged species. Consequently, the synthesized SUHM-MoO_x/NC microspheres exhibited superior lithium-ion storage performance, even at high current densities. It is believed that the facile synthetic strategy for the preparation of unique hollow microspheres using one-pot spray pyrolysis has significant potential for the mass production of hierarchically hollow nanostructures in a wide range of fields, including energy storage.

Declaration of Competing Interest

The authors declare that they have no known competing financial interests or personal relationships that could have appeared to influence the work reported in this paper.

Acknowledgements

This work was supported by a National Research Foundation of Korea (NRF) grant funded by the Korean government (MSIP) (NRF-2021R1A4A2001687, and NRF-2021R1I1A3057700).

Appendix A. Supplementary data

Supplementary data to this article can be found online at https://doi.org/10.1016/j.cej.2022.135536.

References

[1] P. Dou, Z. Cao, J. Zheng, C. Wang, X. Xu, Solid polymer electrolyte coating three-dimensional Sn/Ni bimetallic nanotube arrays for high performance lithium-ion battery anodes, J. Alloys compd. 685 (15) (2016) 690–698.

[2] S.K. Park, J. Lee, S. Bong, B. Jang, K.D. Seong, Y. Piao, A Scalable synthesis of few-layer MoS_2 incorporated into hierarchical porous carbon nanosheets for high-performance Li and Na ion battery anodes, ACS Appl. Mater. Interfaces 8 (30) (2016) 19456–19465.

[3] P. Roy, S.K. Srivastava, Nanostructured anode materials for lithium ion batteries, J. Mater. Chem. A 3 (6) (2015) 2454–2484.

[4] S. Ghosh, S.M. Jeong, S.R. Polaki, A review on metal nitrides/oxynitrides as an emerging supercapacitor electrode beyond oxide, Korean J. Chem. Eng. 35 (7) (2018) 1389–1408.

[5] L. Fan, P. Sun, L. Yang, Z. Xu, J. Han, Facile and scalable synthesis of nitrogen-doped ordered mesoporous carbon for high performance supercapacitors, Korean J. Chem. Eng. 37 (1) (2020) 166–175.

[6] H. Zhang, X. Huang, O. Noonan, L. Zhou, C. Yu, Tailored yolk–shell Sn@C nanoboxes for high-performance lithium storage, Adv. Funct. Mater. 27 (2017) 1606023.

[7] J.-S. Park, J.S. Cho, Y.C. Kang, Nickel vanadate microspheres with numerous nanocavities synthesized by spray drying process as an anode material for Li-ion batteries, J. Alloys Compd. 780 (5) (2019) 326–333.

[8] A. Nulu, V. Nulu, K.Y. Sohn, Silicon and porous MWCNT composite as high capacity anode for lithium-ion batteries, Korean J. Chem. Eng. 37 (10) (2020) 1795–1802.

[9] Y. Liu, N. Zhang, L. Jiao, J. Chen, Tin nanodots encapsulated in porous nitrogen-doped carbon nanofibers as a free-standing anode for advanced sodium-ion batteries, Adv. Mater. 27 (42) (2015) 6702–6707.

[10] Y.S. Jeong, S. Ghosh, J.-K. Kim, D.-W. Kang, S.M. Jeong, C.Y. Kang, J.S. Cho, Multi-channel-contained few-layered $MoSe_2$ nanosheet/N-doped carbon hybrid nanofibers prepared using diethylenetriamine as anodes for high-performance sodium-ion batteries, J. Ind. Eng. Chem. 75 (25) (2019) 100–107.

[11] Y. Wu, Y. Jiang, J. Shi, L. Gu, Y. Yu, Multichannel porous TiO_2 hollow nanofibers with rich oxygen vacancies and high grain boundary density enabling superior sodium storage performance, Small 13 (22) (2017) 1700129.

[12] W. Li, L. Zeng, Z. Yang, L. Gu, J. Wang, X. Liu, J. Cheng, Y. Yu, Free-standing and binder-free sodium-ion electrodes with ultralong cycle life and high rate performance based on porous carbon nanofibers, Nanoscale 6 (2) (2014) 693–698.

[13] H. Yu, J. Yu, S. Liu, S. Mann, Template-free hydrothermal synthesis of CuO/Cu_2O composite hollow microspheres, Chem. Mater. 19 (17) (2007) 4327–4334.

[14] F. Caruso, R.A. Caruso, H. Möhwald, Production of hollow microspheres from nanostructured composite particles, Chem. Mater. 11 (11) (1999) 3309–3314.

[15] J.S. Cho, H.S. Ju, Y.C. Kang, Applying nanoscale kirkendall diffusion for template-free, kilogram-scale production of SnO_2 hollow nanospheres *via* spray drying system, Sci. Rep. 6 (2016) 23915.

[16] J.H. Lee, S.H. Oh, S.Y. Jeong, Y.C. Kang, J.S. Cho, Rattle-type porous Sn/C composite fibers with uniformly distributed nanovoids containing metallic Sn nanoparticles for high-performance anode materials in lithium-ion batteries, Nanoscale 10 (45) (2018) 21483–21491.

[17] J.S. Cho, Y.J. Hong, Y.C. Kang, Design and synthesis of bubble-nanorod-structured Fe_2O_3–carbon nanofibers as advanced anode material for Li-ion batteries, ACS Nano 9 (4) (2015) 4026–4035.

[18] J.S. Cho, Y.C. Kang, All-in-one beaker method for large-scale production of metal oxide hollow nanospheres using nanoscale kirkendall diffusion, ACS Appl. Mater. Interfaces 8 (6) (2016) 3800–3809.

[19] J.S. Cho, Large scale process for low crystalline MoO_3-carbon composite microspheres prepared by one-step spray pyrolysis for anodes in lithium-ion batteries, Nanomaterials 9 (4) (2019) 539.

[20] J.S. Lee, R. Saroha, S.H. Oh, D.H. Shin, S.M. Jeong, J.K. Kim, J.S. Cho, Rational design of perforated bimetallic (Ni, Mo) sulfides/N-doped graphitic carbon composite microspheres as anode materials for superior Na-ion batteries, Small Methods 5 (9) (2021) 2100195.

[21] S.H. Oh, M.S. Jo, S.M. Jeong, Y.C. Kang, J.S. Cho, Hierarchical yolk-shell CNT-(NiCo)O/C microspheres prepared by one-pot spray pyrolysis as anodes in lithium-ion batteries, Chem. Eng. J. 368 (15) (2019) 438–447.

[22] S.H. Oh, S.M. Park, D.-W. Kang, Y.C. Kang, J.S. Cho, Fibrous network of highly integrated carbon nanotubes/MoO_3 composite bundles anchored with MoO_3 nanoplates for superior lithium ion battery anodes, J. Ind. Eng. Chem. 83 (25) (2020) 438–448.

[23] L.Q. Mai, B. Hu, W. Chen, Y.Y. Qi, C.S. Lao, R.S. Yang, Y. Dai, Z.L. Wang, Lithiated MoO_3 nanobelts with greatly improved performance for lithium batteries, Adv. Mater. 19 (21) (2007) 3712–3716.

[24] L. Jin, Y. Qiu, H. Deng, W. Li, H. Li, S. Yang, Hollow $CuFe_2O_4$ spheres encapsulated in carbon shells as an anode material for rechargeable lithium-ion batteries, Electrochem. Acta 56 (25) (2011) 9127–9132.

[25] S.H. Oh, J.K. Kim, Y.C. Kang, J.S. Cho, Three-dimensionally ordered mesoporous multicomponent (Ni, Mo) metal oxide/N-doped carbon composite with superior Li-ion storage performance, Nanoscale 10 (39) (2018) 18734–18741.

[26] C.-P. Wu, K.-X. Xie, J.-P. He, Q.-P. Wang, J.-M. Ma, S. Yang, Q.-H. Wang, SnO_2 quantum dots modified N-doped carbon as high-performance anode for lithium ion batteries by enhanced pseudocapacitance, Rare Metals 40 (2021) 48–56.

[27] J. Wang, Y.-S. Li, P. Liu, F. Wang, Q.-R. Yao, Y.-J. Zou, H.-Y. Zhou, M.-S. Balogun, J.-Q. Deng, Green large-scale production of N/O-dual doping hard carbon derived from bagasse as high-performance anodes for sodium-ion batteries, J. Cent. South Univ. 28 (2021) 361-369.

[28] A. Chithambararaj, A. Chandra Bose, Role of synthesis variables on controlled nucleation and growth of hexagonal molybdenum oxide nanocrystals: investigation on thermal and optical properties, CrystEngComm 16 (2014) 6175–6186.

[29] Y.-J. Lee, T. Lee, A. Soon, Phase stability diagrams of group 6 magnéli oxides and their implications for photon-assisted applications, Chem. Mater. 31 (11) (2019) 4282–4290.

[30] K. Maneelam, C. Saiwan, R. Idem, T. Supap, Ammonia formation in diethylenetriamine-methyldiethanolamine (DETA-MDEA) system in the presence of O_2 during amine-based capture of CO_2 from combustion flue gases, Energy Procedia 114 (2017) 1986–1990.

[31] A. Hartono, E.F.D. Silva, H.F. Svendsen, Kinetics of carbon dioxide absorption in aqueous solution of diethylenetriamine (DETA), Chem. Eng. Sci. 61 (14) (2009) 3205–3213.

[32] T.T.P. Pham, P.H.D. Nguyen, T.T. Vo, C.L. Luu, H.H.P. Nguyen, Preparation of NO-doped β-MoO_3 and its methanol oxidation property, Mater. Chem. Phys. 184 (1) (2016) 5–11.

[33] X. Guan, Y. Ren, S. Chen, J. Yan, G. Wang, H. Zhao, W.u. Zhao, Z. Zhang, Z. Deng, Y. Zhang, Y. Dai, L. Zou, R. Chen, C. Liu, Charge separation and strong adsorption-enhanced MoO_3 visible light photocatalytic performance, J. Mater. Sci. 55 (14) (2020) 5808–5822.

[34] P. Li, X. Yin, Y.a. Yan, K.e. Zhan, J. Yang, B. Zhao, J. Li, Nitrogen-doped graphene-supported molybdenum dioxide electrocatalysts for oxygen reduction reaction, J. Mater. Sci. 53 (8) (2018) 6124–6134.

[35] H. Liu, H. Hu, J. Wang, P. Niehoff, X. He, E. Paillard, D. Eder, M. Winter, J. Li, Hierarchical ternary MoO_2/MoS_2/heteroatom-doped carbon hybrid materials for high-performance lithium-ion storage, ChemElectroChem 3 (6) (2016) 922–932.

[36] S.H. Lim, G.D. Park, D.S. Jung, J.-H. Lee, Y.C. Kang, Towards an efficient anode material for Li-ion batteries: understanding the conversion mechanism of nickel hydroxy chloride with Li- ions, J. Mater. Chem. A 8 (2020) 1939–1946.

[37] S.-K. Park, S.H. Yang, Y.C. Kang, Rational design of metal-organic framework-templated hollow $NiCo_2O_4$ polyhedrons decorated on macroporous CNT microspheres for improved lithium-ion storage properties, Chem. Eng. J. 349 (1) (2018) 214–222.

[38] P. Delporte, C. Pham-Huu, P. Vennegues, M.J. Ledoux, J. Guille, Physical characterization of molybdenum oxycarbide catalyst; TEM, XRD and XPS, Catal. 23 (1995) 251–267.

[39] S. Wang, B. Liu, G. Zhi, G. Xu, Q. Wang, J. Zhang, 2D layered mesoporous MoO_2/rGO composites for high performance anode materials in lithium-ion battery, Microporous Mesoporous Mater. 246 (1) (2017) 14–23.

[40] R. Saroha, J.H. Oh, J.S. Lee, Y.C. Kang, S.M. Jeong, D.-W. Kang, C. Cho, J.S. Cho, Hierarchically porous nanofibers comprising multiple core–shell Co_3O_4@graphitic carbon nanoparticles grafted within N-doped CNTs as functional interlayers for excellent Li–S batteries, Chem. Eng. J. 426 (15) (2021), 130805.

[41] J.S. Cho, J.-S. Park, K.M. Jeon, Y. Chan Kang, 1-D nanostructure comprising porous Fe_2O_3/Se composite nanorods with numerous nanovoids, and their electrochemical properties for use in lithium-ion batteries, J. Mater. Chem. A 5 (21) (2017) 10632–10639.

[42] W.-G. Lim, C. Jo, J. Lee, D.S. Hwang, Simple modification with amine- and hydroxyl- group rich biopolymer on ordered mesoporous carbon/sulfur composite for lithium-sulfur batteries, Korean J. Chem. Eng. 35 (2) (2018) 579–586.

[43] J.Y. Lee, G.D. Park, J.H. Choi, Y.C. Kang, Structural combination of polar hollow microspheres and hierarchical N-doped carbon nanotubes for high-performance Li–S batteries, Nanoscale 12 (3) (2020) 2142–2153.

[44] S.-K. Park, J.-S. Park, Y.C. Kang, Selenium-infiltrated metal–organic framework-derived porous carbon nanofibers comprising interconnected bimodal pores for Li-Se batteries with high capacity and rate performance, J. Mater. Chem. A 6 (3) (2018) 1028–1036.

[45] M.-Q. Wang, C. Tang, C. Ye, J. Duan, C. Li, Y. Chen, S.-J. Bao, M. Xu, Engineering the nanostructure of molybdenum nitride nanodot embedded N-doped porous hollow carbon nanochains for rapid all pH hydrogen evolution, J. Mater. Chem. A 6 (30) (2018) 14734–14741.

[46] Q. Xia, H. Zhao, Z. Du, Z. Zeng, C. Gao, Z. Zhang, X. Du, A. Kulka, K. Świerczek, Facile synthesis of MoO_3/carbon nanobelts as high-performance anode material for lithium ion batteries, Electrochim. Acta 180 (20) (2015) 947–956.

[47] U.K. Sen, S. Mitra, Synthesis of Molybdenum Oxides and their Electrochemical Properties against Li, Energy Procedia 54 (2014) 740–747.

[48] D. Wu, R. Shen, R. Yang, W. Ji, M. Jiang, W. Ding, L. Peng, Mixed molybdenum oxides with superior performances as an advanced anode material for lithium-ion batteries, Sci. Rep. 7 (2017) 44697.

[49] R. Nadimicherla, R. Zha, L. Wei, X. Guo, Single crystalline flowerlike α-MoO_3 nanorods and their application as anode material for lithium-ion batteries, J. Alloys Compd. 687 (5) (2016) 79–86.

[50] S.H. Choi, Y.C. Kang, Fe_3O_4-decorated hollow graphene balls prepared by spray pyrolysis process for ultrafast and long cycle-life lithium ion batteries, Carbon 79 (2014) 58–66.

[51] J. Lin, A.-R.-O. Raji, K. Nan, Z. Peng, Z. Yan, E.L.G. Samuel, D. Natelson, J.M. Tour, Iron oxide nanoparticle and graphene nanoribbon composite as an anode material for high-performance Li-ion batteries, Adv. Funct. Mater. 24 (14) (2014) 2044–2048.

[52] W. Wei, S. Yang, H. Zhou, I. Lieberwirth, X. Feng, K. Müllen, 3D graphene foams cross-linked with pre-encapsulated Fe_3O_4 nanospheres for enhanced lithium storage, Adv. Mater. 25 (21) (2013) 2909–2914.

[53] J.S. Lee, M.S. Jo, R. Saroha, D.S. Jung, Y.H. Seon, J.S. Lee, Y.C. Kang, D.-W. Kang, J.S. Cho, Hierarchically well-developed porous graphene nanofibers comprising N-doped graphitic C-coated cobalt oxide hollow nanospheres as anodes for high-rate Li-ion batteries, Small 16 (32) (2020) 2002213.

[54] J.Q. Huang, T.Z. Zhuang, Q. Zhang, H.J. Peng, C.M. Chen, F. Wei, Permselective graphene oxide membrane for highly stable and anti-self-discharge lithium–sulfur batteries, ACS Nano 9 (3) (2015) 3002–3011.

[55] J. Mei, T. He, Q. Zhang, T. Liao, A. Du, G.A. Ayoko, Z. Sun, Carbon–phosphorus bonds-enriched 3D graphene by self-sacrificing black phosphorus nanosheets for elevating capacitive lithium storage, ACS Appl. Mater. Interfaces 12 (19) (2020) 21720–21729.

[56] H. Kim, K. Lim, G. Yoon, J.-H. Park, K. Ku, H.-D. Lim, Y.-E. Sung, K. Kang, Exploiting lithium–ether Co-intercalation in graphite for high-power lithium-ion batteries, Adv. Energy Mater. 7 (19) (2017) 1700418.

[57] L.-B. Tang, B. Zhang, C.-S. An, H. Li, B. Xiao, J.-H. Li, Z.-J. He, J.-C. Zheng, Ultrahigh-rate behavior anode materials of $MoSe_2$ nanosheets anchored on dual-heteroatoms functionalized graphene for sodium-ion batteries, Inorg. Chem. 58 (12) (2019) 8169–8178.

[58] H. Zhang, H. He, J. Luan, X. Huang, Y. Tang, H. Wang, Adjusting the yolk–shell structure of carbon spheres to boost the capacitive K^+ storage ability, J. Mater. Chem. A 6 (2018) 23318–23325.

[59] S.Y. Jeong, J.S. Cho, Porous hybrid nanofibers comprising $ZnSe/CoSe_2$/carbon with uniformly distributed pores as anodes for high-performance sodium-ion batteries, Nanomaterials 9 (10) (2019) 1362.

[60] J.-S. Park, J.S. Cho, Y.C. Kang, Scalable synthesis of $NiMoO_4$ microspheres with numerous empty nanovoids as an advanced anode material for Li-ion batteries, J. Power Sources 379 (1) (2018) 278–287.